Agricultural and Forest Meteorology 249 (2018) 149–162

Contents lists available at ScienceDirect

Agricultural and Forest Meteorology

journal homepage: www.elsevier.com/locate/agrformet

Climate change enhances the severity and variability of drought in the Pearl River Basin in South China in the 21st century

Zhaoli Wang[a,b], Ruida Zhong[a], Chengguang Lai[a,b,*], Zhaoyang Zeng[a], Yanqing Lian[c], Xiaoyan Bai[d]

[a] School of Civil Engineering and Transportation, South China University of Technology, Guangzhou, 510641, China
[b] State Key Lab of Subtropical Building Science, South China University of Technology, Guangzhou, 510641, China
[c] Institute of Natural Resources Sustainability, University of Illinois at Urbana-Champaign, 2204 Griffith Drive, Champaign, IL, 61820, USA
[d] Department of Environmental Engineering, School of Environmental Science and Engineering, Guangdong University of Technology, Guangzhou, 510006, China

ARTICLE INFO

Keywords:
Future drought
Spatiotemporal variation
VIC
PDSI
General circulation models
Pearl River Basin

ABSTRACT

Drought is expected to increase in frequency, severity, and duration in the future due to global warming and this will greatly threaten the future socio-economic development. This study evaluates the spatiotemporal variation of future drought (2016–2100) in the Pearl River Basin (PRB) using the Palmer drought severity index (PDSI), the Variable Infiltration Capacity (VIC) model, and future climate projections based on the general circulation models (GCMs) from phase 5 of the Coupled Model Intercomparison Project (CMIP5) under three representative concentration pathway (RCP) scenarios. The results show that future drought conditions are expected to be more serious than historical (1960–2015) drought conditions in the PRB, especially under RCP8.5. The severity and variability of future drought conditions are also higher than for the historical period. The west Guangxi and South Guizhou provinces exhibit the highest increment in drought severity under the three RCP scenarios. At the seasonal scale, drought severity shows the highest increment in the winter with little change in summer; the summer drought severity increases in most areas of the PRB but the increment of the drought severity is lower than the winter. The number of future drought events is expected to decrease but the duration and severity are expected to increase, especially in the mid-west PRB and under high greenhouse gas (GHG) emission scenarios. In summary, in most areas of the PRB, the severity and variability of drought are expected to increase in the 21 st century, especially in the mid-west PRB and an increase in evapotranspiration is assumed to be the main underlying cause. Irrigation projects and agricultural production in the PRB might face serious threats of drought in the future.

1. Introduction

Drought is one of the most frequent and hazardous disasters worldwide and has caused considerable agricultural and economic losses (Mishra and Singh, 2010; Piao, 2010; Lobell and Costa-Roberts, 2011). Recent global surface air temperatures have risen significantly due to global climate change and increases in greenhouse gas (GHG) emissions, which are expected to exacerbate future drought events (Dai, 2013; Cook et al., 2014). The 4th and 5th Assessment Report of the Intergovernmental Panel on Climate Change (IPCC) (AR4 and AR5) has predicted an increase in global surface air temperatures of 0.3 ~ 4.8 °C and associated changes in the spatial patterns of global precipitation in the 21st century. If global temperatures continue to rise, the area and intensity of drought may change dramatically.

General circulation models (GCMs), released by the Coupled Model Intercomparison Project (CMIP), provide information on long-term future climate projections (IPCC, 2013). The GCMs simulate different preset scenarios representing different future GHG emission levels and provide excellent tools for evaluating future changes in drought conditions. As the latest release of the GCM data by the CMIP, the CMIP Phase 5 project (CMIP5) provides more than 50 GCMs for the IPCC's AR5 from 24 institutes around the world (Taylor et al., 2011). The representative concentration pathway (RCP) scenarios (Moss et al., 2010) that include four scenarios (i.e., RCP2.6, RCP4.5, RCP6.0, and RCP8) with increasing levels of GHG emissions were adopted in the CMIP5 as well as the IPCC AR5. Using these GCMs, many studies have demonstrated an increase in future drought severities with increasing levels of GHG emissions (Wang, 2005; Sheffield and Wood, 2008; Li et al., 2012; Dai, 2011, 2013; Cook et al., 2014; Wang and Chen, 2014). These studies have characterized a general outline of future drought changes and pointed out the subsequent direction of the effort. However, most studies have only focused on a national or global scale,

* Corresponding author at: School of Civil Engineering and Transportation, South China University of Technology, Guangzhou, 510641, China.
E-mail address: laichg@scut.edu.cn (C. Lai).

https://doi.org/10.1016/j.agrformet.2017.12.077
Received 9 September 2017; Received in revised form 30 November 2017; Accepted 3 December 2017
Available online 12 December 2017
0168-1923/ © 2017 Elsevier B.V. All rights reserved.

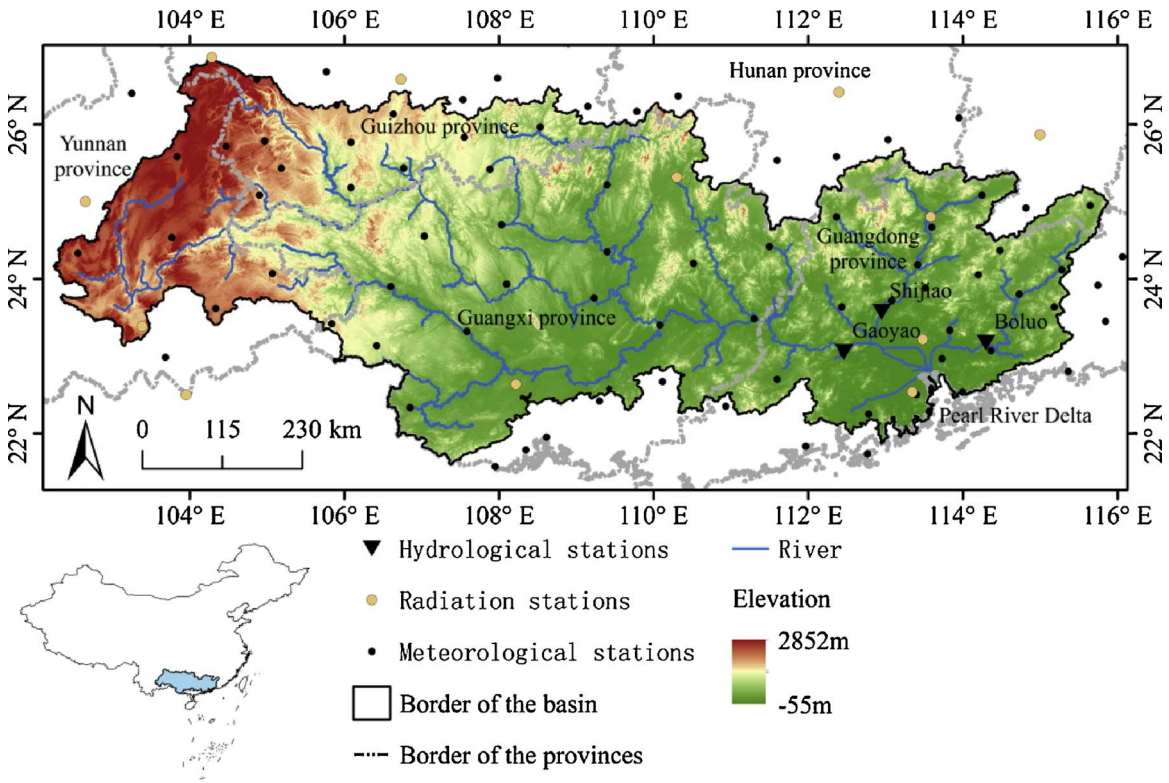

Fig. 1. Location, topography and stations of the Pearl River Basin (PRB).

impeding further understanding of varying patterns at a fine scale and applications. First, a coarse spatial resolution is usually inadequate for revealing the spatiotemporal pattern of a regional drought because only a fine spatial resolution enables the regional management of drought control, water resource allocation, and agricultural production. Second, the drought metrics that were used in the earlier studies, such as the standardized precipitation evapotranspiration index (SPEI) (Vicente-Serrano et al., 2010) and the conventional Palmer drought severity index (PDSI) (Palmer, 1965), did not consider land surface factors (e.g., hydrological process, soil property, and vegetation), resulting in a lack of clarity regarding key change in future drought events.

It is well known that the conventional PDSI is calculated based on the water balance and thus has been widely applied to the study about climate change and impact on drought (Sheffield and Wood, 2008; Cook et al., 2014; Dai, 2013; Wang and Chen, 2014). However, in the conventional PDSI, the water budget is calculated using a simple two-layer bucket-type water balance model that does not consider land use and the spatial heterogeneity of soil properties (Zhang et al., 2012a,2012b). Despite a revision of the PDSI using a self-calibrating algorithm (scPDSI, Wells et al., 2004) to improve the portability and spatial comparability, the index is still inadequate for determining the actual drought conditions in detail. To solve this problem, distributed hydrological models that feature improved physical mechanisms and a wider consideration of land surface processes have been used to analyze drought change (Wu et al., 2011; Zhang et al., 2012a,b; Liu et al., 2015; Zhang and He, 2016). For example, Zhang et al. (2012a,2012b) and Liu et al. (2015) improved the PDSI by replacing the conventional two-layer bucket-type model with the variable infiltration capacity (VIC) hydrological model (Liang et al., 1994); in this approach the water budget of PDSI is calculated based on the VIC model's outputs (e.g. evapotranspiration, soil moisture, and runoff yield). This improvement represents a new direction for a more reliable evaluation of drought conditions.

As a widely used and grid-based macroscale distributed hydrological model, the VIC model not only simulates the land surface hydrological processes based on water and energy balances but also considers several other factors such as the sub-gridcell heterogeneity of the land cover, the root zone of the vegetation, and frozen soil. The model has been widely validated in different climatic regions, including arid and humid regions in China, and has been coupled successfully with downscaled GCMs to obtain future land surface process projections (Wu et al., 2014; Yan et al., 2015). Moreover, evidence has proved the reliability and rationality of this model based on calculations of the water budget of the PDSI (Wu et al., 2011; Zhang et al., 2012a,2012b; Liu et al., 2015; Zhang and He, 2016). Because it considers not only soil moisture but also evapotranspiration, the VIC-based PDSI is assumed to be a powerful tool for analyzing the future changes in drought conditions.

Even though the Pearl River Basin (PRB) is located in the subtropical humid monsoon region of South China, the area has suffered considerably from frequent and severe meteorological drought events. For example, a rare severe drought (the most severe drought disaster in China since 1951, Barriopedro et al., 2012) occurred in the upper PRB located in southwest China from the autumn of 2009 to the spring of 2010, causing an economic loss of more than 3.5 billion dollars and a crop loss of more than 1 million ha. A consensus has been reached that the historical droughts occurring in the PRB can be attributed to decreased precipitation (Barriopedro et al., 2012). However, a debate remains as to the factors driving the evolution and changes in future droughts events although Cook et al. (2014) believed that increased evapotranspiration in South China was a key factor. Therefore, further explorations of the major influencing factors on future drought events in the PRB are required.

In this study, the VIC model was used to calculate the VIC-based PDSI in the PRB for the evaluation of future drought conditions. Detailed objectives of the study include 1) to construct the VIC-based PDSI in the PRB, 2) to simulate the hydrological processes in a future period (2016–2100) using the VIC model with a downscaled multi-model ensemble (MME) of the GCM projections and calculate the PDSI based on the VIC outputs, and 3) to evaluate the spatiotemporal

variation of future drought conditions in the 21st century (2016–2100).

2. Study area and data

2.1. Study area

The Pearl River is the second largest river in China and has an annual mean streamflow of $34.9 \times 10^{10} m^3/a$. The PRB (Fig. 1) is located in the subtropical humid monsoon zone of South China and covers the Yunnan, Guizhou, Guangxi, and Guangdong provinces (102.2–115.9°E, 21.6–26.9°N). It has a drainage area of about $45.4 \times 10^4 km^2$ and elevations ranging from −55 m to 2852 m. The annual mean precipitation of the PRB is 1554 mm and the annual mean air temperature ranges from 14 °C to 22 °C. The middle-upper area of the PRB, especially the junction of the Yunnan, Guizhou, and Guangxi provinces has a typical karst landform that exhibits a spreading trend (Jiang et al., 2014; Lai et al., 2016). The Pearl River Delta is facing a serious water shortage problem because of rapid urbanization and population explosion (Liu et al., 2017). Potential and enormous threats induced by drought exist due to the widespread karst landform, highly developed economy, and dense population; therefore, a systematic projection of future drought conditions in the PRB is vital.

2.2. Data

2.2.1. Meteorological and hydrological observations

Meteorological and hydrological data for the period of 1959–2015 were collected for calibration of the VIC model, downscaling and multi-model merging of the GCMs, and hydrological simulation in the historical period respectively. Ninety-one meteorological stations in or around the PRB (Fig. 1) provided meteorological observations of air temperature, air pressure, wind speed, vapor pressure (VP), and daily sunshine duration (SSD). The incoming short-wave and long-wave radiation data required by the VIC model were estimated based on SSD, air temperature, and VP using the Angstrom formula (Martinezlozano et al., 1985) and the Konzelmann formula (Konzelmann et al., 1994) respectively. Shortwave radiation observations from 11 radiation stations in the PRB were used to estimate the coefficients a and b of the Angstrom formula (Martinezlozano et al., 1985) used to calculate the incoming shortwave radiation based on the SSD.

The precipitation observations were derived from the China Gauge-based Daily Precipitation Analysis (CGDPA) dataset (Shen and Xiong, 2015) provided by the Chinese Meteorological Administration (CMA). CGDPA is a gridded daily precipitation dataset with a spatial resolution of 0.25° × 0.25° and is generated by more than 2400 gauge stations across mainland China using the optimal interpolation (OI) method. The CGDPA features high accuracy and stability in South China because of the high density of the gauge stations and the strict quality control (Shen and Xiong, 2015). The precipitation dataset was interpolated to result in the same spatial scale as the VIC model by bilinear interpolation; the other meteorological data were interpolated using the kriging method.

Monthly streamflow observations during 1960–2000 were collected from three hydrological stations in the PRB (i.e., Gaoyao, Shijiao, and Boluo) for calibration and validation. The three hydrological stations correspond to the three main sub-basins of the PRB, which include the Xijiang, Beijiang, and Dongjiang River Basins, respectively. For this study, March to May are regarded as spring, June to August as summer, September to November as autumn, and December to February of next year as winter.

2.2.2. CMIP5 projections

The future climate projections were derived from six GCMs (esgf-data.dkrz.de) participating in the CMIP5: CanESM2, CNRM-CM5, CSIRO-Mk3.6, MIROC-ESM, MPI-ESM-LR, and MRI-CGCM3 (Table 1). These GCMs were selected due to the good simulation performance regarding precipitation and air temperature and the convenience of providing meteorological forcing data required by the VIC model. The MPI-ESM-LR, CanESM2, and MIROC-ESM models have performed well in air temperature simulations in China (Chen and Frauenfeld, 2014), while the CNRM-CM5, MRI-CGCM3, and CSIRO-Mk3.6 models have performed well in precipitation simulations in South China (Huang et al., 2013).

The climate projection variables that were used to force the VIC model included precipitation, surface air temperature, near-surface wind speed, sea level pressure, near-surface relative humidity, surface longwave and longwave radiations. Most of the data can be used directly as VIC model input; however, the sea level pressure has to be converted to the actual air pressure based on elevation and air temperature and the relative humidity has to be converted to VP based on the maximum and minimum air temperatures using Food and Agriculture Organization (FAO) Eq. (19) (Huang et al., 2013). The daily climate data of the GCMs in the historical period (1960–2015) and the future period (2016–2100) under different RCP scenarios were obtained with the purpose of downscaling and multi-model merging as well as developing the future hydrological simulation respectively. Only the RCP2.6, RCP4.5, and RCP8.5 scenarios were selected after discovering that some GCM variables were unavailable for the RCP6.0 scenario.

3. Methodology

3.1. VIC hydrological model

The VIC macroscale distributed hydrological model (Liang et al., 1994) is a grid-based land surface processes-based scheme based on water and energy balances. The soil column of the model is divided vertically into three layers, in which the top two layers represent the response of the soil moisture to the rainfall events, while the bottom layer represents the seasonal soil moisture behavior (Liang et al., 1996). The evapotranspiration model consists of three parts: canopy evaporation, vegetation transpiration, and soil water evaporation. The surface runoff portion of the model is only generated from the top two soil layers and is based on the variable infiltration curve; the underground baseflow is only generated from the bottom soil layer based on the Arno baseflow formulation (Franchini and Pacciani, 1991; Liang et al., 1994). The potential evapotranspiration (PET) is calculated by the FAO56 Penman-Monteith (PM) equation (Allen et al., 1998), which is also used to calculate the reference crop evapotranspiration (ET0). The VIC model has been successfully applied in the PRB for soil moisture and streamflow simulations (Niu et al., 2015; Niu and Chen, 2016) and for coupling with the GCMs (Wu et al., 2014; Yan et al., 2015).

The latest VIC 5.0 (http://vic.readthedocs.io/en/master/) model was used and applied at a spatial resolution of 0.1° × 0.1°. The soil parameters of the model were derived from the FAO's Harmonized World Soil Database (HWSD) 1-km spatial resolution global soil classification and texture dataset (FAO et al., 2009), which was converted to soil hydraulic parameters via the formulas developed by Saxton and Rawls (2006). The land cover parameters were derived from the China land use remote sensing monitoring database (http://www.resdc.cn) (Liu, 2005). The land cover data of 1990, 2000, and 2010 were used for the hydrological simulations for the different historical periods (1960–1995, 1996–2005, and 2006–2015 respectively). This study also assumed that the land cover of the PRB would not significantly change in the future and used the land cover data of 2015 for the hydrological simulation during 2016–2100.

The VIC model was calibrated by adjusting the parameters until the simulated streamflow values satisfactorily fit the observed streamflow values. Since the model only provides runoff yield data, a routing model (Lohmann et al., 1996) was used to couple with the VIC model to generate the streamflow values at the outlets of the basins. Two widely-used performance indices, the Nash–Sutcliffe coefficient of efficiency (NSCE) and the relative bias (BIAS) were used to evaluate the

Table 1
List of the selected GCMs.

	GCM	Institution	Resolution
1	CanESM2	Canadian Centre for Climate Modelling and Analysis, Canada	128 × 64
2	CNRM-CM5	Centre National de Recherches Météorologiques, France	256 × 128
3	CSIRO-Mk3.6	Commonwealth Scientific and Industrial Research Organization/Bureau of Meteorology, Australia	192 × 96
4	MIROC-ESM	Atmosphere and Ocean Research Institute (The University of Tokyo), National Institute for Environmental Studies, and Japan Agency for Marine-Earth Science and Technology, Japan	128 × 64
5	MPI-ESM-LR	Max Planck Institute for Meteorology, Germany	192 × 96
6	MRI-CGCM3	Meteorological Research Institute, Japan	320 × 160

hydrological simulation performance of the VIC model:

$$NSCE = 1 - \frac{\sum_{i=1}^{n} (O_i - S_i)^2}{\sum_{i=1}^{n} (O_i - \overline{O})^2} \quad (1)$$

$$BIAS = \left(1 - \frac{\sum_{i=1}^{n} S_i}{\sum_{i=1}^{n} O_i}\right) \times 100\% \quad (2)$$

where O_i and S_i are the observed and simulated streamflow time series values and $\overline{O}$ is the mean value of O_i. The NSCE describes the agreement between the observed and simulated values for the streamflow time series, while the BIAS describes the systematic error of the simulated streamflow values.

In this study, the VIC model was calibrated at the three hydrological stations (i.e. Gaoyao, Shijiao, and Boluo) during the calibration period (1960–1980) by means of optimizing the NSCE of the simulated streamflow and maintaining the simulation bias in a reasonable range. Since the VIC model usually requires great computation time and has relatively less parameters to be calibrated, similar with the study of Xie et al. (2007), we calibrated the model by optimizing each parameter separately. Subsequently, the calibrated model was run during the validation period (1981–2000) to validate the calibrated results to evaluate the applicability of the model.

3.2. PDSI based on VIC model and self-calibrating procedure

The PDSI is based on the concept of climatically appropriate for existing conditions (CAFEC) developed by Palmer (1965). The calculation includes two parts: the calculation of *d*, with *d* defined as the water deficiency, and the climatological standardization of *d*. *d* is the difference between the actual precipitation *P* and the CAFEC precipitation P^ (i.e. P − P^). P^ can be understood as the amount of precipitation required to maintain a normal soil moisture level (Zhang and He, 2016). It is calculated by several potential and actual water budget components including PET, potential soil water recharge (PR), potential runoff (PRO), potential soil water loss (PL), actual evapotranspiration (ET), actual soil water recharge (R), actual runoff (RO), and actual soil water loss (L):

$$\hat{P}_i = \alpha_m PET_i + \beta_m PR_i + \gamma_m PRO_i - \delta_m PL_i \quad (3)$$

$$\begin{cases} \alpha_m = \overline{ET_m}/\overline{PET_m} \\ \beta_m = \overline{R}_m/\overline{PR}_m \\ \gamma_m = \overline{RO}_m/\overline{PRO}_m \\ \delta_m = \overline{L}_m/\overline{PL}_m \end{cases} \quad (4)$$

where *i* means the i^{th} time step (normally monthly); α_m, β_m, γ_m, and δ_m are the climatological coefficients of the month *m* (ranging from 1 to 12) and are the ratio of the annual mean values of the actual and potential water budget components in the month *m*.

The PDSI was calculated at monthly scale in this study. The calculation steps of the water budget components were based on earlier studies (Alley, 1984; Liu et al., 2015; Palmer, 1965; Zhang et al., 2012a,2012b). The VIC model provides several daily output variables for the water budget calculation including PET, actual evapotranspiration, soil moisture of each soil layer, surface runoff, and baseflow. The PET, ET, initial soil moisture ($S_1 \sim S_3$), and the soil moisture variation ($\Delta S_1 \sim \Delta S_3$) of the three soil layers were retrieved from the daily output variables of the VIC model. In our study, the middle and bottom soil layers of the model are relatively thick, especially the bottom layer, which is thicker than 1.0 m. Because the bottom layer may not be related to the crop yields, only the top and middle soil layers were considered for calculating the *PR*, *R*, *PL,* and *L*:

$$PR = max(AWC - (S_1 + S_2), 0) \quad (5)$$

$$R = max(\Delta S_1 + \Delta S_2, 0) \quad (6)$$

$$PL = PL_s - PL_u \quad (7)$$

$$PL_s = min(PET, S_1) \quad (8)$$

$$PL_u = (PET - PL_s)S_2/AWC \quad (9)$$

$$L = max(-(\Delta S_1 + \Delta S_2), 0) \quad (10)$$

where the *AWC* is the total available water capacity (mm) of the top and the middle soil layers; PL_s and PL_u are the *PL* of the top and the middle layer respectively. Here the field capacity was used as the *AWC*.

To maintain the water balance, the infiltration from the middle soil layer to the bottom soil layer was considered a part of the RO. Since the bottom soil layer of the model only generates the baseflow, the RO is calculated as:

$$RO = RO_s + \Delta S_3 + RO_u \quad (11)$$

where the RO_s is the surface runoff; RO_u is the underground baseflow; ΔS_3 is the soil moisture variation of the bottom soil layer. The PRO is calculated by the traditional formula:

$$PRO = S_1 + S_2 \quad (12)$$

The climatological standardization of *d* aims to use *d* as a standardized drought index that considers local climate and drought duration; the self-calibrating procedure of Wells et al. (2004) was used:

$$Z_i = K_1 \cdot K_2 \cdot d_i \quad (13)$$

$$X_1 = qZ_1 \quad (14)$$

$$X_i = pX_{i-1} + qZ_i \quad (15)$$

where Z_i is the moisture anomaly index of the i^{th} time step; K_1 is the temporal correction weight; K_2 is the spatial correction weight; *p* and *q* are the duration factors; and X_i is the PDSI value of the i^{th} time step. Wells et al. (2004) modified the calculation of K_2, *p,* and *q*, in which K_2 is calculated by assigning a certain frequency (normally 0.02) for the extreme wet (PDSI > 4) and dry (PDSI < − 4) events. For more details about the calculation of K_1, K_2, *p,* and *q,* please refer to Wells et al. (2004).

Since the climatological coefficients and other parameters of the PDSI are essentially the indicators of the local climate, this study firstly calculated the PDSI of the PRB based on the VIC model outputs in the historical period (1960–2015) and thereby obtained the climatological coefficients (α_m, β_m, γ_m, δ_m), correction weight (K_1, K_2), and duration

factors (p and q). Thereafter, we fixed the above parameters and then calculated the PDSI with these parameters using the VIC model outputs for the future period (2016–2100), aiming to evaluate the impact of climate change on the drought changes of the PRB more reasonably. The above processes allow for comparing the temporal changes between the historical and future periods.

3.3. Downscaling and multi-model ensemble methods

Since the horizontal resolutions of the GCMs are too coarse (mostly > 100km) to reveal the regional and local climate characteristics, the downscaling methods were essential to generate the climate projections at a finer scale to facilitate the assessment of local impacts. Currently, the Delta downscaling method is more prevalent than the dynamic method and the traditional statistical downscaling methods because the Delta method requires less computing resources and input data and generates a higher spatial resolution for future climate projections (Wang and Chen, 2014; Peng et al., 2017). The bias-corrected climate imprint (*Bcc*I) method (Werner and Cannon, 2015), one of the Delta methods, has been widely applied for downscaling the GCMs. This method includes a bias correction process based on the climate imprint (CI) method (Hunter and Meentemeyer, 2005). Despite being similar to the bias correction spatial disaggregation (BCSD) method (Brekke et al., 2013), the *Bcc*I first downscales the GCMs and then corrects the bias while the BCSD employs the reverse procedure. More details about this method can be found in the studies of Peng et al. (2017) and Wang and Chen (2014). Additionally, the bias correction process of the *Bcc*I is a process of quantile delta mapping (Cannon et al., 2015) based on the cumulative density function (CDF).

High variability and uncertainty usually exist among the future projections of the GCMs due to their different implementations and initial states. In this case, a single GCM is inadequate to provide a stable and reliable future climate projection (Asseng et al., 2013; Wang et al., 2017a,2017b). To solve this problem, obtaining a robust MME projection by merging several GCMs is an effective approach (Krishnamurti et al., 2000; Murphy et al., 2004). The Bayesian model average (BMA) method (Raftery et al., 2005; Min and Hense, 2006) is an optimal method for generating a relatively robust MME from the GCMs and was applied in this study. The BMA is a statistical method that combines models by using the weighted average values of the models and in which the weights are estimated based on the maximum likelihood method. Details on the BMA method can be found in several studies (Raftery et al., 2005; Min and Hense, 2006; Wang et al., 2017a,b).

3.4. Quantification of drought severity and characterization of drought event

Drought severity is defined as the impact of drought events or the shortage of water storage during drought events (Xu et al., 2015). To be more exact, this factor is usually calculated as the spatial or temporal integral of the drought intensity. In this study, we interpreted the drought intensity as the absolute value of the drought index under drought conditions (PDSI ≤ -1):

$$I = \begin{cases} |\mathrm{PDSI}|, \ PDSI \leq -1 \\ 0, \ PDSI > -1 \end{cases} \tag{16}$$

where I is defined as the drought intensity. To evaluate the spatiotemporal variation of drought, this study calculated the annual drought severity at both the gridcell scale and the basin scale. The gridcell-scale annual drought severity was calculated as:

$$S_a = \sum_{m=1}^{12} I_{a,m} \tag{17}$$

where S_a is the drought severity (unit: month) in the year a of a gridcell and $I_{a,m}$ is the drought intensity in the year a and the month m. The basin-wide annual drought severity was calculated as:

$$S_a = \sum_{m=1}^{12} \sum_{x} \sum_{y} A_{x,y} \cdot I_{x,y,a,m} \tag{18}$$

where S_a is the annual basin-wide drought severity in the year a; $I_{x,y,a,m}$ is the drought intensity in the year a and the month m at the gridcell with the coordinate x and y; $A_{x,y}$ is the area of this gridcell. Here the unit of the S_a is km^2·month.

The theory of runs (Yevjevich and Ingenieur, 1967; Ayantobo et al., 2017) was used to identify and characterize the drought events of the gridcells. A continuous time series of the PDSI in drought condition (PDSI < -1) is regarded as a drought event. The duration and severity, the two main characteristics of a drought event, are the length of the time series and the time integral of the corresponding drought intensity respectively. For details, please refer to the study by Ayantobo et al. (2017).

4. Results and analysis

4.1. Evaluation of the VIC model performance and the downscaled MME

Fig. 2 shows that the monthly NSCEs of the three stations in the calibration and validation periods are higher than 0.85; the NSCEs of the Gaoyao and Shijiao stations are even higher than 0.95 and all the BIASes are lower than 3%. The results indicate that the VIC model performs satisfactorily for the hydrological simulation and maintains a reasonable water balance, demonstrating that the calibrated model can be used for the calculation of the PDSI and for coupling with the GCMs.

Subsequently, the performance of the downscaled MME generated by the *Bcc*I and the BMA methods was evaluated. Here only the downscaling and MME results of the monthly precipitation and air temperature were evaluated because they are the top two key meteorological factors of drought (Zhang et al., 2013). Table 2 shows that the MME based on the BMA method exhibits a higher correlation and lower bias than each individual GCM for both precipitation and air temperature with satisfactory correlation coefficients (0.826 for precipitation and 0.98 for air temperature) and almost no bias. Fig. 3 also indicates that the MME method has a narrower range of Pearson correlation coefficient (CC) and bias among the gridcells than the individual GCMs, indicating a better simulation performances and higher stability of the MME method. Therefore, the climate projections for the BMA-based MME method show great potential as an input to the VIC model.

4.2. Spatiotemporal variation of future drought

The VIC model was run for the future period (2016–2100) driven by daily climate projections of the MME method under three scenarios (i.e. RCP2.6, 4.5, and 8.5) and the PDSI was calculated using the model outputs. The historical PDSI values calculated based on the climate observations during 1960–2015 were used as the reference. Fig. 4 shows the frequency of the PDSIs representing different dry and wet events during the historical and future periods. Apparently, the frequency of the dry events (PDSI < -1) was higher for the future period than for the historical period. Moreover, for the future period, the frequency of the “severe drought” and “extreme drought” events (corresponding to $-4 <$ PDSI ≤ -3 and PDSI ≤ -4 respectively) is higher for the high-emission scenario (i.e. RCP8.5) than for the lower emission scenario, indicating that the future drought condition would be more serious and that the drought severity is expected to be higher under higher GHG emission levels.

Fig. 5 presents the curves of the basin-wide average PDSI and drought severity in the historical period (1960–2015) and the future period (2016–2100). Clearly, future drought conditions are expected to be more serious under the three scenarios with lower basin-averaged

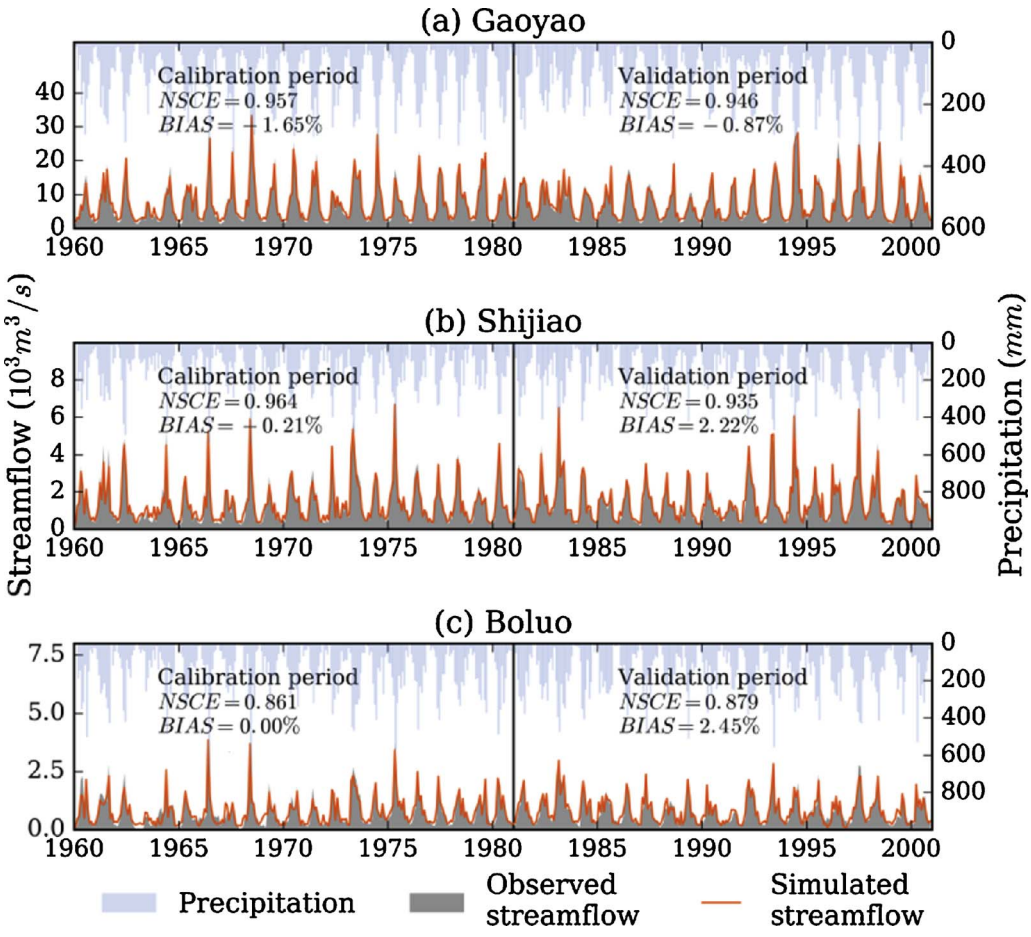

Fig. 2. Calibration and validation results of the VIC model.

Table 2
Pearson correlation coefficients (CCs) and biases of the basin-wide downscaled monthly precipitation and temperature from the GCMs and MMEs.

GCMs	Monthly precipitation		Monthly air temperature	
	CC	Bias (%)	CC	Bias (°C)
CanESM2	0.700	−0.10	0.962	0.02
CNRM-CM5	0.750	−0.15	0.966	−0.02
CSIRO-Mk3.6	0.690	0.69	0.960	0.02
MIROC-ESM	0.680	−0.73	0.958	0.01
MPI-ESM-LR	0.715	0.61	0.964	−0.01
MRI-CGCM3	0.726	0.54	0.965	−0.01
MME_AM	0.812	0.14	0.979	0.01
MME_BMA	0.826	0.04	0.980	0.01

Note: MME_AM represents MME by the arithmetic mean method; MME_BMA represents MME by the BMA method; CC and Bias represent Pearson correlation coefficient and relative bias respectively.

PDSI values (PDSI < 0) and higher drought severity. Fig. 5 also indicates that the drought trend and drought severity begin to increase in the late 1990s. Generally, the basin-wide PDSI values and drought severity of the three RCP scenarios show little differences in magnitude, which increases the reliability of the occurrence of future drought events.

Fig. 6 shows the spatial distribution of the gridcell-scale annual mean drought severity in the historical and future periods under the three RCP scenarios. Clearly, the drought severity shows significantly different spatial patterns for the two periods. The values and variability of the future drought severity are higher than in the historical period. In the future period, areas located in the middle-upper PRB exhibit the highest drought severity while the Pearl River Delta shows the lowest drought severity. The three RCP scenarios result in similar spatial patterns of drought severity although there are differences in magnitude. The RCP8.5 results in higher values in the upper PRB and lower values in the Pearl River Delta than the RCP2.6, indicating that increased GHG emissions will further increase the drought severity.

To explore the future spatiotemporal changes in more detail, we analyzed the drought severity variability in different periods (i.e. 2016–2040, 2041–2070, 2071–2100, and 2016–2100) under three RCP scenarios. Generally, similar spatial patterns are observed for the variability in the future drought severity in the different periods (Fig. 6). Except for the Pearl River Delta that exhibits decreased drought severity, most areas show increased drought severity in different periods under the three scenarios, among which RCP8.5 results in the greatest increases (Fig. 7).

Fig. 8 shows the boxplot of annual mean drought severity of the gridcells in different periods. Since the drought severity increased after the late 1990s (Fig. 5), the annual mean drought severity of the historical period was calculated separately for two periods (1960–1995 and 1996–2015) to present the changes in historical drought. Apparently, the magnitude and spatial variation range of the drought severity increased from 1960 to 1995 to 1996–2015 and would further increase during the first half of the 21st century. Under RCP2.6, the drought severity and its spatial variation increased from 2016 to 2040 to 2041–2070 and then decreased slightly during 2071–2100, which could be related to the decreasing trend of the GHG emissions after the middle 21st century. By comparison, under RCP4.5 and RCP 8.5, the drought severity and spatial variation exhibit a continuously increasing trend during the 21st century, in which RCP8.5 results in the highest drought severity and spatial variation during 2071–2100. During 2071–2100, the median of the RCP8.5 scenario is almost twice the value of the drought severity during 1960–1995. Generally, the severity and spatial

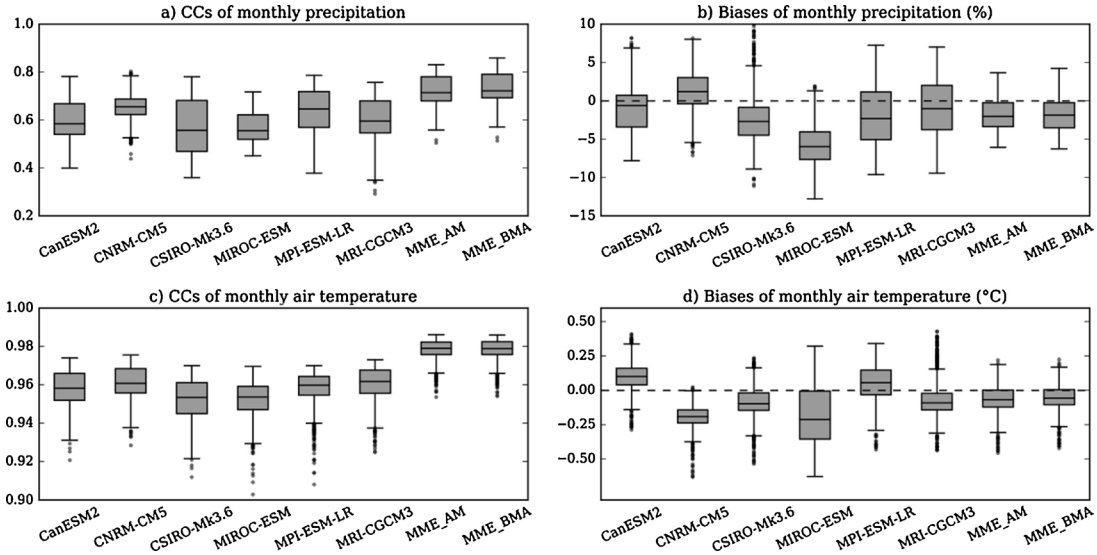

Fig. 3. Boxplot of Pearson correlation coefficients (CCs) and biases of monthly precipitation and air temperature of the GCMs and MMEs at gridcell scale. Note: the upper and lower edges of the box represent the quantiles of 75% and 25% respectively; the horizontal line in the box represent s the median value; the upper and lower horizontal lines out of the box represent s the maximum and minimum respectively; the outer points represents the outliers; MME_AM represents MME by the arithmetic mean method; MME_BMA represents MME by the BMA method; CC and Bias represent Pearson correlation coefficient and relative bias respectively.

variation of the drought show an increasing trend during 2016–2100, especially under RCP8.5.

Because different crops grow in different seasons, the future drought severity variation in the PRB was further explored for different seasons. The difference between the annual mean drought severity for the future (2016–2100) and the historical period (1960–2015) is summarized in Fig. 9. Generally, the changes in the drought severity exhibit quite different magnitudes and spatial patterns for the four seasons. In spring, the drought severity generally decreases in the mid-east of the PRB, especially in and around the Pearl River Delta, while increases are observed in the west, especially the western Guangxi province. The summer drought severity shows relatively little change across the entire PRB. In autumn, the increasing drought severity covers most areas of the PRB, with high values distributed in the mid-east areas, including the middle Guangxi province and the southern Guizhou province. In winter, a sharp increase in drought severity occurs in the west Guangxi province while a decrease in drought severity is observed in the Pearl River Delta. Additionally, Fig. 9 indicates that all three RCP scenarios result in similar spatial patterns in the same season and higher emission scenarios generally result in higher values.

4.3. Changes in duration and severity of drought events

Here we evaluate how the duration and the severity of the drought events change in the future. Based on the run theory, the drought events were identified first and their duration and the severity were calculated for the gridcells in the historical and future periods.

Fig. 10 shows the spatial distribution of the number of drought events per decade, the ratio of drought duration (i.e. the ratio of the time in a drought condition and the total time of the gridcell), the mean duration, and the drought severity of the drought events in the historical and future periods under the RCP scenarios. The number of drought events decreases from 12 to 16 per 10 a in the historical period to 10–13 per 10 a in the future period. Inversely, the ratio of drought duration and mean duration of drought events increases in the future period. The ratio of drought duration ranges from 0.3 to 0.5 in the historical period and increases significantly to more than 0.5 in the future period, reaching 0.7 or higher in the mid-west PRB, especially under RCP4.5 and RCP8.5. The mean duration of drought events also increases from generally less than 5 months to more than 6–9 months in the future with even higher values (more than 12 months) in the mid-west PRB, especially under RCP4.5 and RCP8.5. The mean severity of the drought events has highly similar spatial patterns as the mean duration of the

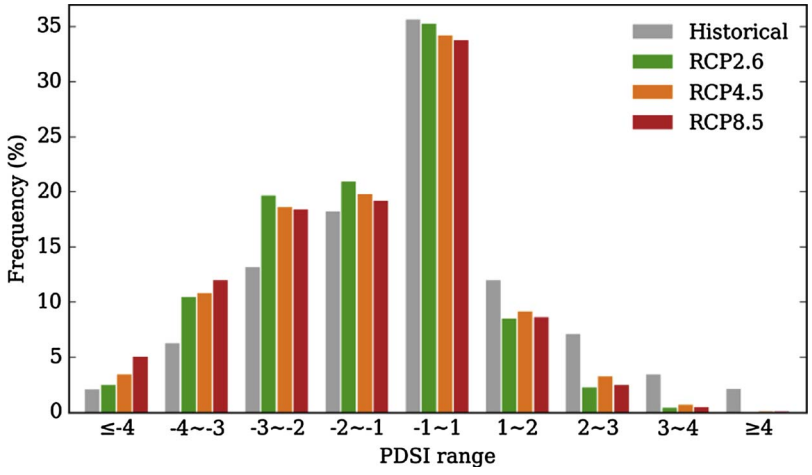

Fig. 4. Frequency of PDSIs representing different dry or wet events. Note: $PDSI \leq -4$: extreme drought; $-4 < PDSI \leq -3$: severe drought; $-3 < PDSI \leq -2$: moderate drought; $-2 < PDSI \leq -1$: mild drought; $-1 < PDSI \leq 1$: normal; $1 < PDSI \leq 2$: mild wet; $2 < PDSI \leq 3$: moderate wet; $3 < PDSI \leq 4$: severe wet; $PDSI \geq 4$: extreme wet.

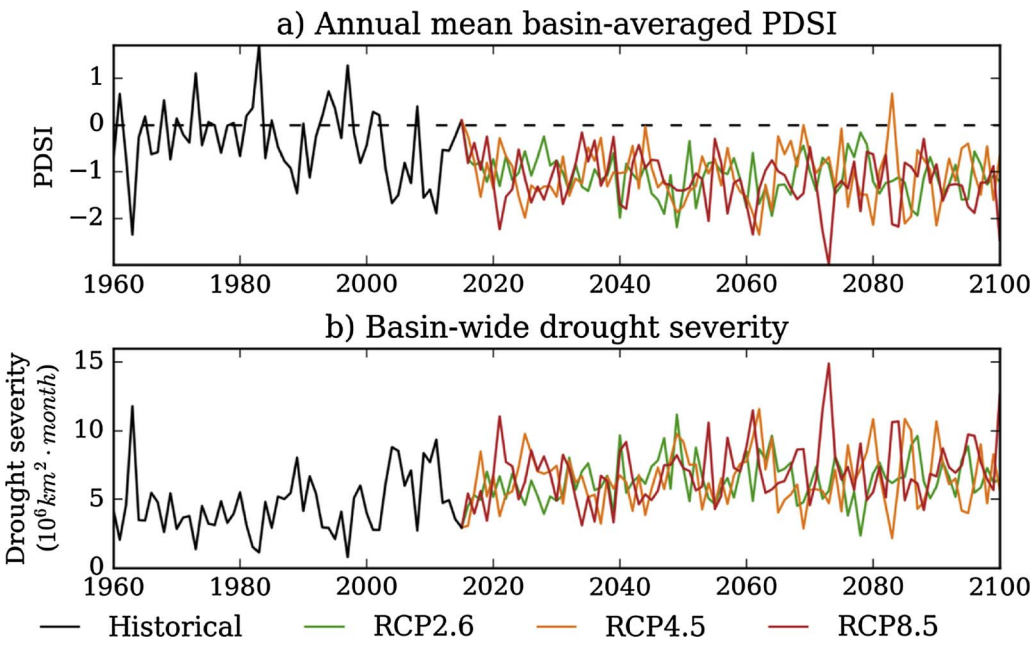

Fig. 5. Time series of annual basin-wide PDSI and drought severity between the historical and future period.

drought events under different RCP scenarios, indicating that large increases in the drought severity may be related to the increased drought duration. Generally, the drought events in the PRB, especially the mid-west PRB, show a trend of large-scale drought events with longer duration and higher severity in the future.

To explore the variation of the drought events in the future and the relationship between their duration and severity, the frequency and mean severity of the drought events with different durations were calculated. As the frequency of the drought events with a duration of more than 12 months is quite small, here only the drought events with a duration of fewer than 12 months are displayed. Fig. 11aa shows that the distribution of drought events with different durations is quite different for the historical and future periods and that the frequency of the intermediate-term drought events (4–9 months) is apparently higher in the future. In the historical period, the frequency of the drought events generally decreases as the duration increases and the short-term drought events (1–3 months) feature the highest frequency. For the future period, the intermediate −term drought events have a higher frequency than the short-term drought events and the drought events of 7–9 months have a higher frequency for RCP8.5 than for the RCP2.6 and RCP4.5 scenarios. Additionally, as shown in Fig. 11b, the mean severity of the drought events exhibits a strong correlation with the duration and there is little difference in the severity-duration curves between the historical and future periods under the three RCP scenarios; this indicates that different scenarios have little effect on the change in the severity-duration relationships. It is inferred that the increase in the drought severity in the PRB in the future is mainly attributed to longer drought durations.

5. Discussion

Sheffield et al. (2012) suggested that in studies on drought change responses to climate change, the change in drought was overestimated in the past decades because the PET was overestimated due to using a simplified estimation model. However, Dai (2013) argued that drought events have increased over the past decades. The two contradictory views were believed to result from the use of different precipitation datasets and the limitation of the conventional PDSI (Trenberth et al.,

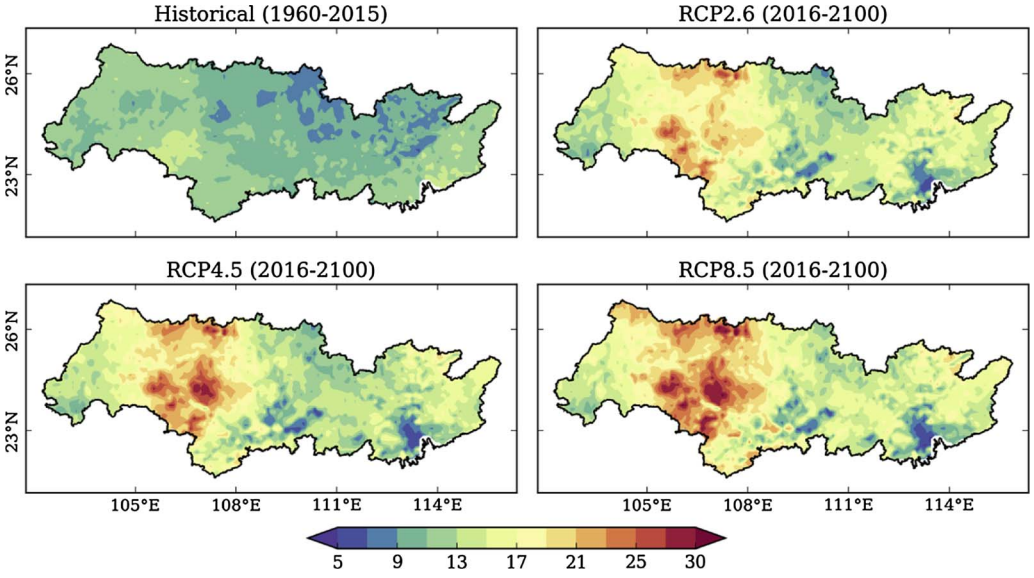

Fig. 6. Spatial distribution of annual mean drought severity (month) between historical and future period.

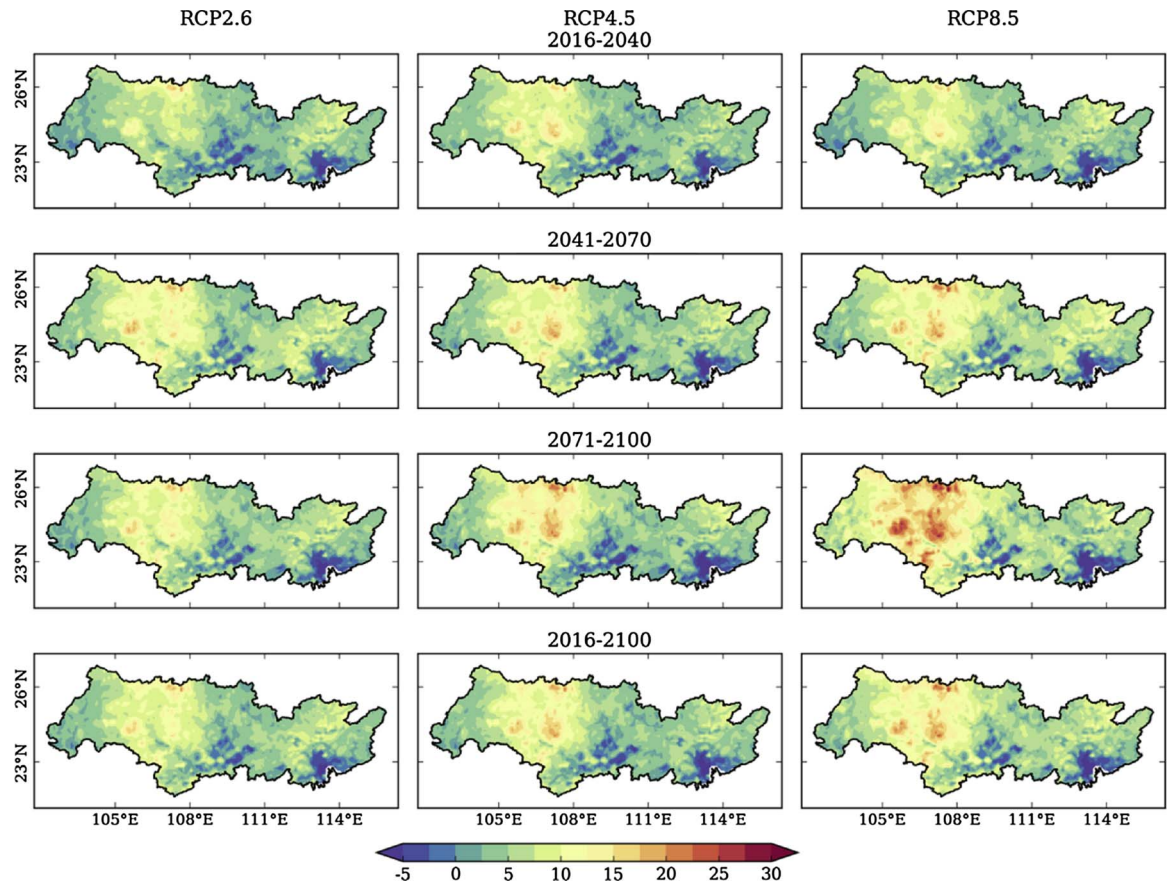

Fig. 7. Spatial distribution of annual mean drought severity variation (month) of periods under three scenarios.

2014). In this case, the usage of the VIC model, which considers meteorological and land surface factors with reliable physical mechanisms for PDSI calculation may be a better choice. For the 21st century, an increasing drought trend has been consistently observed both at regional and global scales, including the PRB (Wang, 2005; Sheffield and Wood, 2008; Dai, 2013; Cook et al., 2014; Wang and Chen, 2014; Touma et al., 2015; Venkataraman et al., 2016), although the drought metrics used in these studies are different. For example, Dai (2013) suggested that the changes in soil moisture and the conventional scPDSI of seasonal change result in similar future drought trends in the PRB. Wang (2005) found that more severe droughts would increase in the winter in the PRB. Wang and Chen (2014) predicted that southwestern China (including the upper PRB) will be one of the regions with a sharply decreased PDSI in the future. Although the drought trends and magnitudes presented in this study differ slightly from the above-mentioned studies due to a different usage of the drought metrics and the methods, the historical and future evaluations are generally consistent. Therefore, the projected drought conditions presented in this study are, to some extent, adequate to serve as references for agricultural production and water resource planning in the PRB.

Widespread karst landforms and precipitation anomalies have traditionally been considered the main reasons for drought in the PRB, especially in the upstream area (i.e. southwest China) (Barriopedro et al., 2012; Zhang et al., 2013; Jiang et al., 2014). However, as air temperatures have significantly increased due to climate change, evapotranspiration may play a more important role for future drought conditions (Vicente-Serrano et al., 2010; Dai, 2013; Cook et al., 2014; Touma et al., 2015; Venkataraman et al., 2016). For example, a

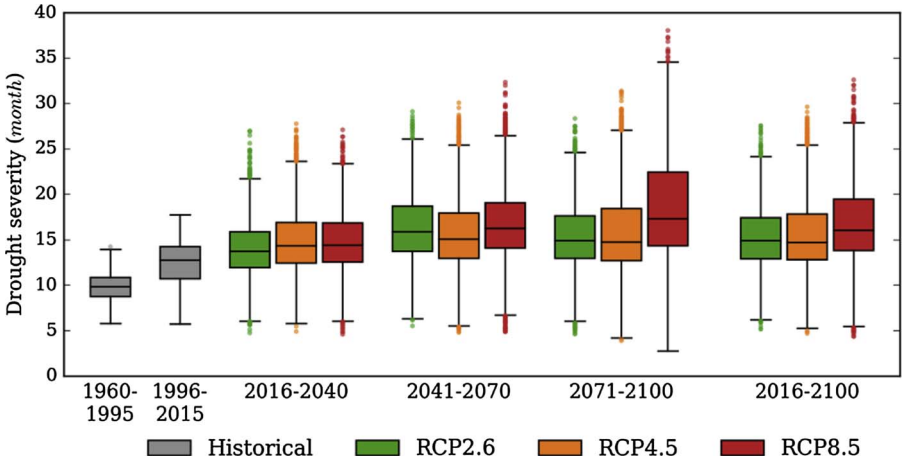

Fig. 8. Boxplot of annual mean drought severity (month) of the gridcells in different periods.

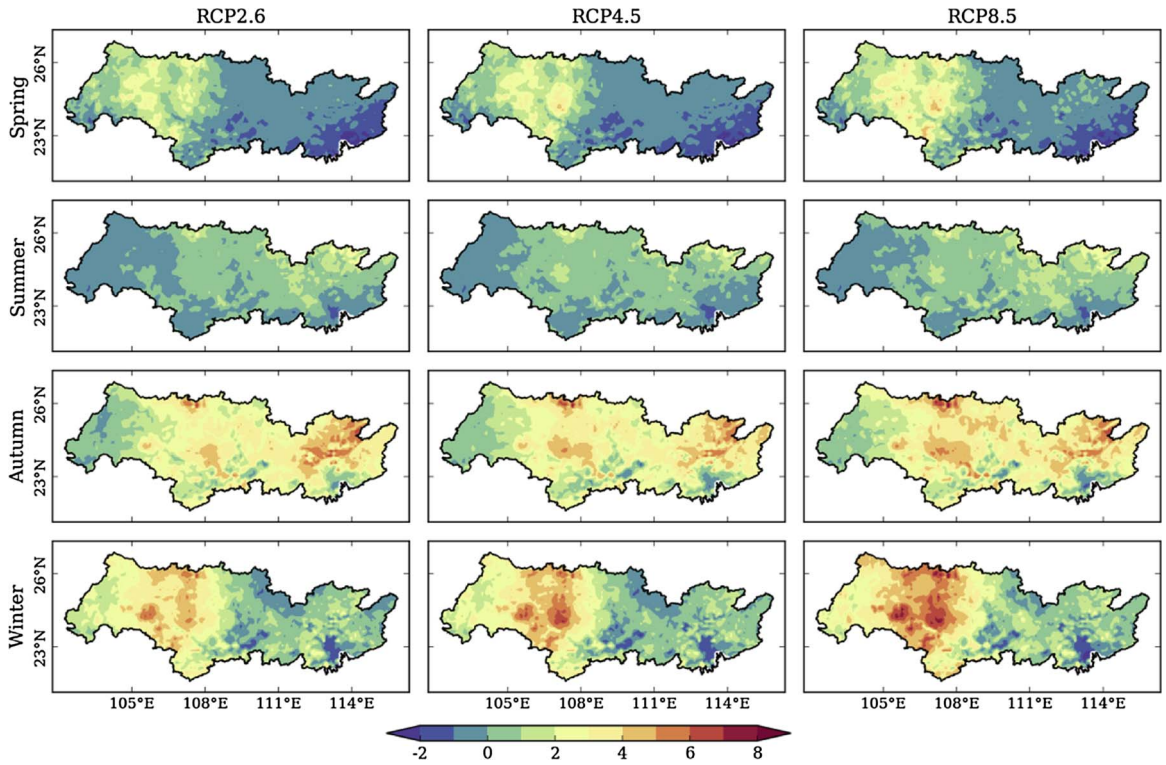

Fig. 9. Spatial difference of annual mean drought severity between the future and historical period in four seasons under three scenarios.

regional study (Wang et al., 2011) found that agricultural drought is more sensitive to climate change as the air temperature increases; the increased evaporation will have the largest impact on the drought over the north mid-high latitudes (Dai, 2013). Cook et al. (2014) argued that PET dominates the future drought in southeast China. It is necessary to clarify whether the drought variation is mainly caused by a change in precipitation or evapotranspiration because decreased precipitation usually means a lower water supply while increased evapotranspiration means higher irrigation water demand (Wang et al., 2017a,b). Therefore, the contribution of both precipitation and PET to future drought change requires further discussion.

Fig. 12 shows the temporal change of the precipitation and the PET in the PRB. Fig. 12a indicates that the precipitation features a non-significant trend in the historical and future periods. However, the PET shows an increasing trend after the late 1990s (Fig. 12b) and a high-emission scenario (RCP8.5) results in a higher increment than the lower emission scenarios (RCP2.6 and RCP4.5). Based on this observation, the increasing trend of the PET after the late 1990s might be the main reason behind the increasing trend of the drought.

Figs. 13 and 14 display the spatial patterns of the future changes in the seasonal and annual precipitation and the PET respectively. The PET consistently exhibits high increments across the PRB, especially in spring and winter. In contrast, the precipitation shows quite different trends and spatial patterns in different seasons; in spring and winter,

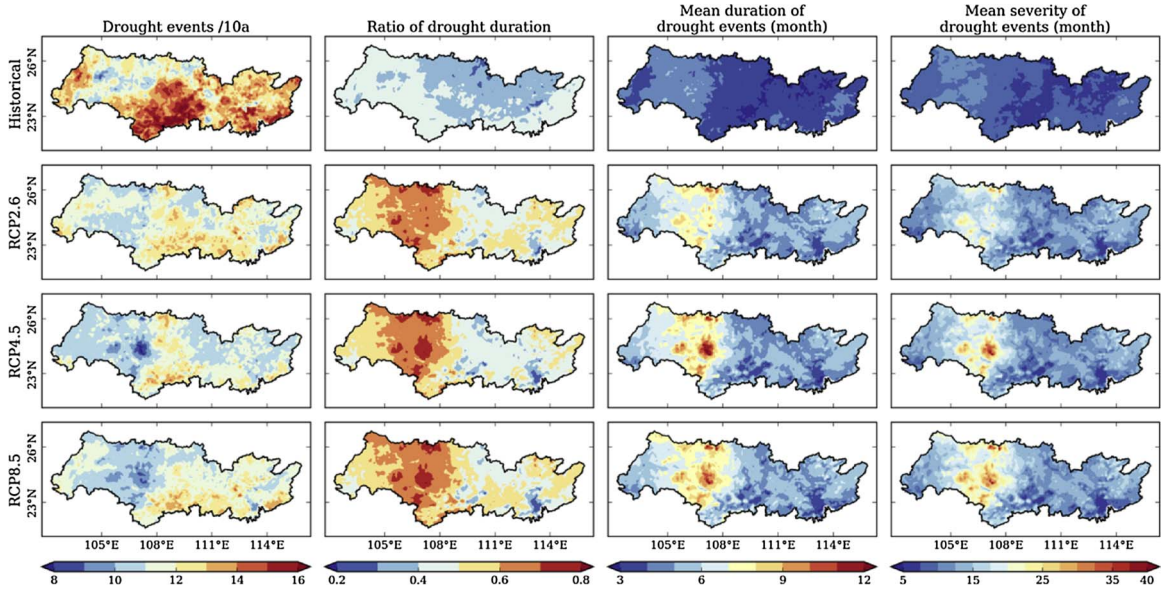

Fig. 10. Spatial distribution of number of drought events per decade, ratio of the drought duration, mean duration and severity of the drought events both in the historical and future period.

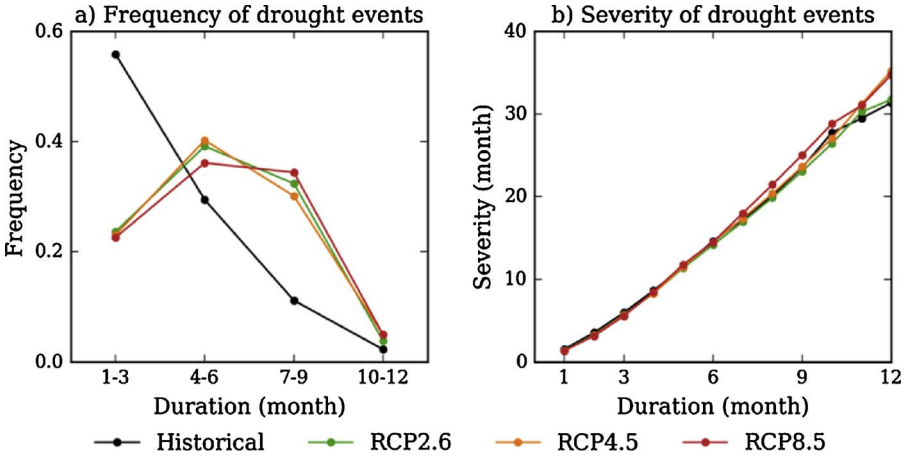

Fig. 11. Frequency (a) and mean severity (b) of drought events with different durations both in historical and future period.

increased precipitation is observed while decreased precipitation occurred in summer and autumn. Therefore, the inducer of the future drought may be different for spring and winter than for summer and autumn. In summer and autumn, the PET increases (by 10% ~ 30%) while the precipitation decreases (by 5% ~ 15%) in the future. However, based on the data in Fig. 9, the drought severity slightly increases in summer but widely increases in autumn in the future period. Since the PRB is a subtropical monsoon region, the abundant summer rainfall is still adequate to offset the increased evapotranspiration, which may be the main reason for the relatively little change in the drought severity in summer. As for autumn, the spatial distributions of the change in the precipitation and the PET are similar to the corresponding drought severity variation; therefore, the future increased drought severity in the autumn may be induced by a coupling of the decreased precipitation and evapotranspiration. Note that the decrease in the precipitation in autumn is apparently higher under RCP2.6; therefore, the autumn drought may be related to precipitation to a greater degree under the lower emission scenario. In spring and winter, both precipitation and PET increase in most areas of the PRB in the future (Fig. 13 and Fig. 14). Hence, the increased drought severity in spring and winter may be largely a result of the increased evapotranspiration. In winter, the precipitation increases by 30% ~ 40% in the eastern PRB but only increases by 20% and even decreases (under RCP8.5) in the west PRB. By comparison, the PET increases sharply in winter, especially in the mid-west PRB; therefore, the winter drought of the PRB in the future may be dominated by the increased evapotranspiration, especially in the mid-west PRB. As for spring, the spatial distribution of the precipitation and the PET changes are different (Fig. 13 and Fig. 14). The increases in precipitation in the mid-west PRB (15% ~ 35%) in spring are higher than in the east PRB (5% ~ 25%), while the increases in PET in the mid-west PRB (0% ~ 30%) are lower than in the east PRB (30% ~ 40%). However, according to Fig. 9, the drought severity increases in the west PRB but slightly decreases in the east PRB in the spring, indicating that the west PRB may still face a more severe spring drought in the future although the precipitation increases more than the PET. Since the evapotranspiration is not the only factor considered by the VIC-based PDSI, which also takes the soil properties and the runoff yield into account, the increased drought severity in the future may also result from the relatively weak water-holding ability in the west PRB, where widespread karst landforms are common. However, in the spring, the PET has a greater contribution to the increased drought than the precipitation.

In short, consistent with the results of Cook et al. (2014), evapotranspiration rather than precipitation is generally the primary factor increasing the drought severity of the PRB, especially in the winter. This means that the PRB, especially the mid-west PRB, would face a more severe demand for irrigation water demand in the future, which may largely affect agricultural production. As the main crop in the PRB is rice, which generally yields twice per year, the increased PET in the spring would have a deleterious impact on the sowing of the first crop in the spring; in addition, the increased PET in the autumn also would affect the harvest of the second crop in the winter in the PRB. Along

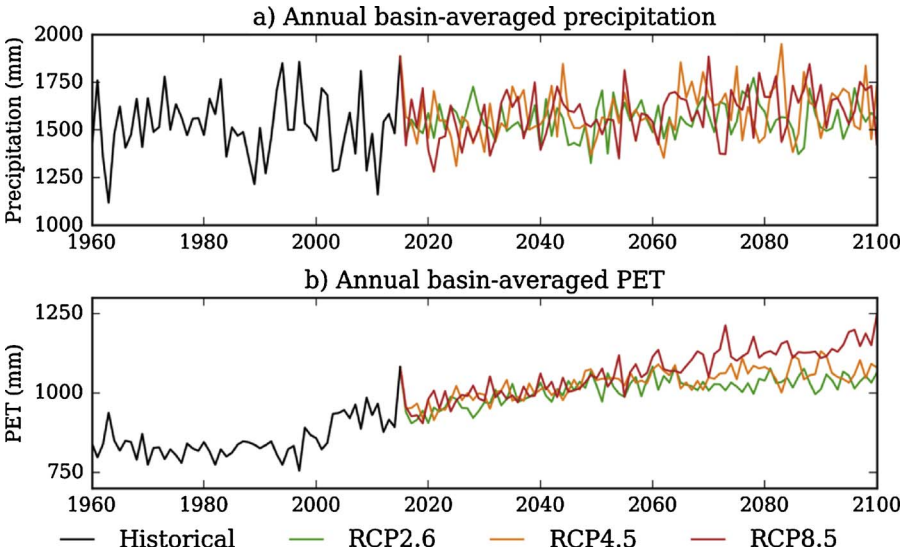

Fig. 12. Annual basin-wide precipitation and PET both in the historical and future period.

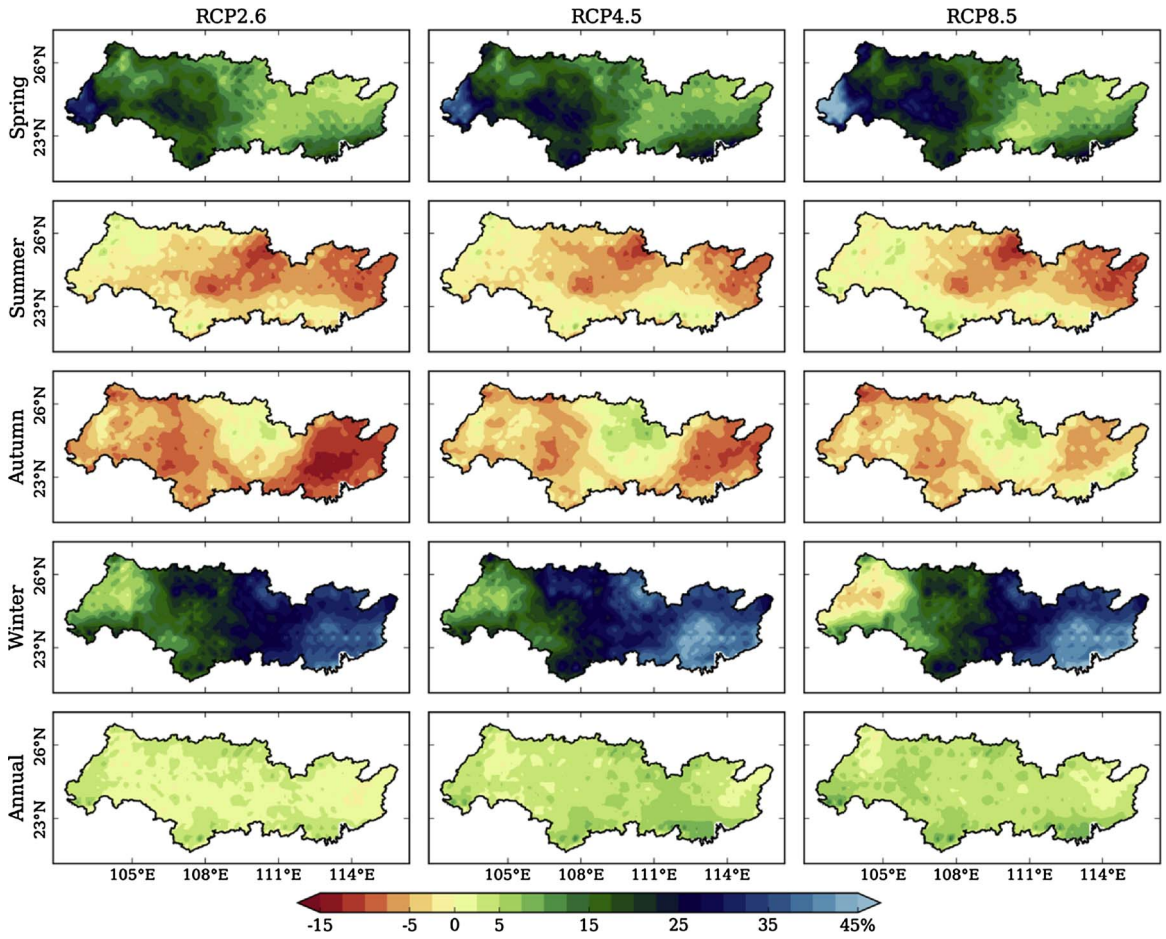

Fig. 13. Spatial distribution of precipitation difference (%) between future and historical period at seasonal and annual scal.

with the increases in the GHG emissions, the impact of the increased carbon dioxide (CO_2) on the vegetation and crop production should not be neglected (Cao et al., 2010; Wiltshire et al., 2013), as the increased CO_2 may increase the water use efficiency of plants and thus reduce the evapotranspiration (Cook et al., 2014). However, related studies have found that a CO_2 fertilization effect on the rice yield could not compensate for the negative impact of the increased temperature (Wang et al., 2017a,b). Generally, with the increased drought conditions driven by increasing evapotranspiration under climate change, the stress on irrigation and crop production in the PRB may be more serious in the future and some corrective and preventative actions should be considered.

6. Conclusions

This study evaluated and predicted the spatiotemporal changes in future (2016–2100) drought conditions in the PRB under climate change using six CMIP5 GCM projections under three RCP scenarios and the VIC-based PDSI model.

Drought conditions in the PRB will become more serious in the future period compared to the historical period (1960–2015), especially under RCP8.5. The future drought severity has higher values and greater spatial variation than the historical drought under different RCP scenarios. The greatest changes in the future drought severity occur in the west Guangxi and south Guizhou provinces, in which RCP8.5 generally results in the most severe drought severities. Under RCP2.6, the drought severity reaches the highest level during 2041–2070; in contrast, under RCP4.5 and RCP8.5, the drought severity continuously increases and RCP8.5 results in the highest drought severity and variation during 2071–2100. Seasonally, the drought severity shows the least change in summer while the most serious aggregation occurs in the mid-west PRB in winter. In autumn, the increment of the drought severity is lower than in the winter but covers the largest area with high values. The occurrence of future drought events in the PRB generally decreases but the duration and severity of the drought events increase, especially in the mid-west PRB under RCP8.5. The increased drought severity in the future is mainly attributed to a lengthened drought duration. In most areas of the PRB, especially the mid-west PRB, the drought areas are expected to increase in size and the drought severity and variation are projected to increase in the 21st century. Along with the increase in the drought severity driven by higher evapotranspiration and the lengthening of the drought duration, the PRB may have to face increased demands for irrigation and negative effects on agricultural production in the future under climate change.

Generally, this study provides a reference to evaluate and predict the spatiotemporal changes in future drought conditions at basin scale using different CMIP5 GCM projections scenarios and the VIC-based PDSI model, which may be significant for prevention and reduction, water resources planning, and agricultural management.

Acknowledgements

The research is financially supported by the National Natural Science Foundation of China (Grant No. 51579105, 51709117, 91547202, 51479216, 51509040), China Postdoctoral Science Foundation (2017M612662), the Water Resource Science and Technology Innovation Program of Guangdong Province (2016-25), the Science and Technology Program of Guangzhou City (201707010072), the Science and Technology Planning Project of Guangdong Province, China (2017A040405020) and the special fund of water resources

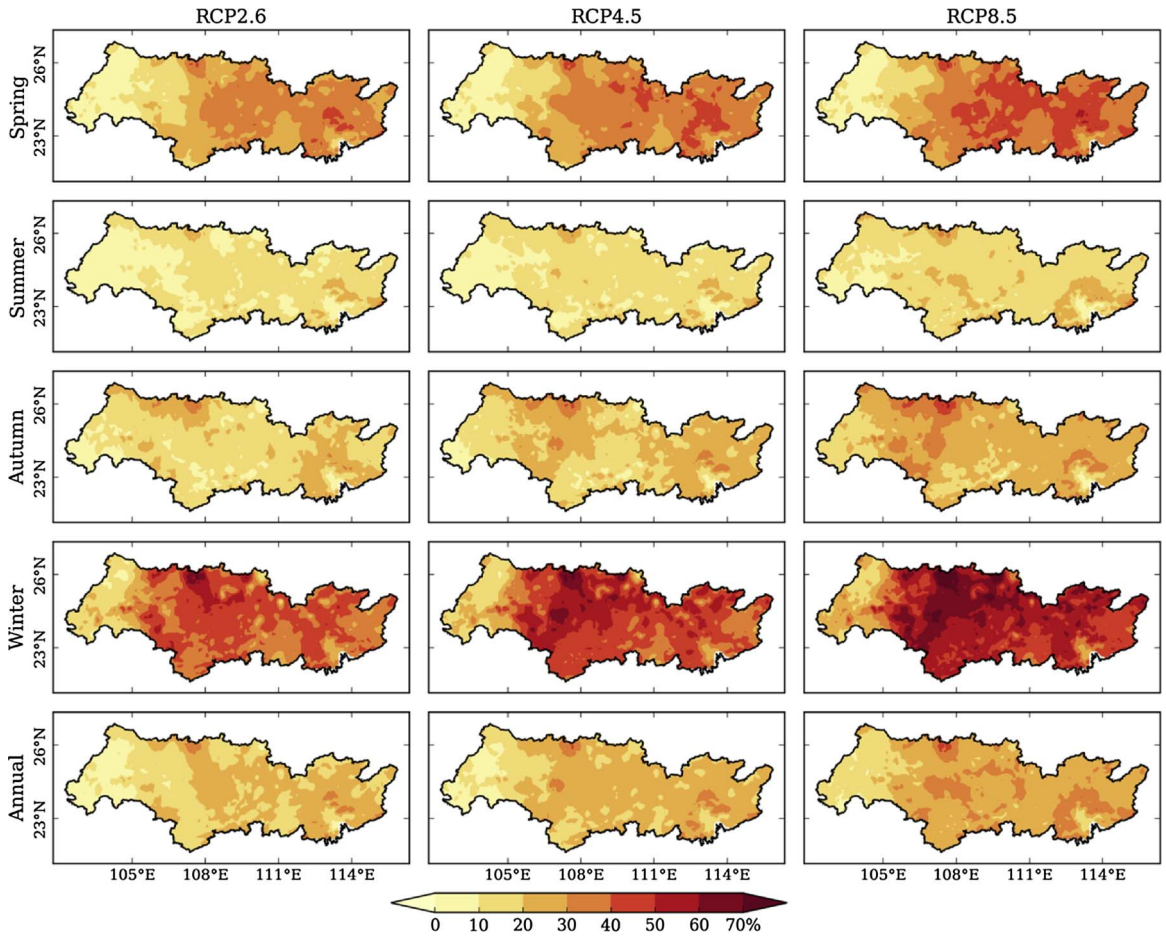

Fig. 14. Spatial distribution of PET difference (%) between future and historical period at seasonal and annual scale.

conservation and protection of Guangdong Province(2017).

References

Allen R.G., Pereira L.S., Raes D. and Smith M., 1998. Crop Evapotranspiration-Guidelines for computing crop water requirements. Food and Agricultural Organization of the United Nations Irrigation and Drainage Paper, 56 300 (8): D05109.

Alley, W.M., 1984. The palmer drought severity index: limitations and assumptions. J. Appl. Meteorol. 23 (23), 1100–1109.

Asseng, S., et al., 2013. Uncertainty in simulating wheat yields under climate change. Nat. Clim. Change 3 (9), 827–832.

Ayantobo, O.O., Li, Y., Song, S., Yao, N., 2017. Spatial comparability of drought characteristics and related return periods in mainland China over 1961–2013. J. Hydrol. 550, 549–567.

Barriopedro, D., Gouveia, C.M., Trigo, R.M., Wang, L., 2012. The 2009/10 drought in China: possible causes and impacts on vegetation. J. Hydrometeorol. 13 (4), 1251–1267.

Brekke, L., Thrasher, B., Maurer, E., Pruitt, T., 2013. Downscaled CMIP3 and CMIP5 Climate and Hydrology Projections: Release of Downscaled CMIP5 Climate Projections, Comparison with Preceding Information, and Summary of User Needs. US Dept. of the Interior, Bureau of Reclamation, Technical Services Center, Denver, Colorado.

Cannon, A.J., Sobie, S.R., Murdock, T.Q., 2015. Bias correction of GCM precipitation by quantile mapping: how well do methods preserve changes in quantiles and extremes? J. Clim. 28 (17).

Cao, L., Bala, G., Caldeira, K., Nemani, R., Ban-Weiss, G., 2010. Importance of carbon dioxide physiological forcing to future climate change. Proc. Natl. Acad. Sci. U. S. A. 107 (21), 9513–9518.

Chen, L., Frauenfeld, O.W., 2014. Surface air temperature changes over the twentieth and twenty-First centuries in China simulated by 20 CMIP5 models. J. Clim. 27 (11), 3920–3937.

Cook, B.I., Smerdon, J.E., Seager, R., Coats, S., 2014. Global warming and 21st century drying. Clim. Dyn. 43 (9–10), 2607–2627.

Dai, A., 2011. Characteristics and trends in various forms of the Palmer Drought Severity Index during 1900–2008. J. Geophys. Res. 116 (D12), 1248–1256.

Dai, A., 2013. Increasing drought under global warming in observations and models. Nature Clim. Change 3 (2), 171.

FAO, IIASA, ISRIC, ISSCAS, 2009. Harmonized World Soil Database Version 1.1.

Franchini, M., Pacciani, M., 1991. Comparative analysis of several conceptual rainfall-runoff models. J. Hydrol. 122 (1-4), 161–219.

Huang, D.Q., Zhu, J., Zhang, Y.C., Huang, A.N., 2013. Uncertainties on the simulated summer precipitation over Eastern China from the CMIP5 models. J. Geophys. Res-Atmos. 118 (16), 9035–9047.

Hunter, R.D., Meentemeyer, R.K., 2005. Climatologically aided mapping of daily precipitation and temperature. J. Appl. Meteorol. 44 (10), 1501–1510.

IPCC, 2013. Climate Change 2013: The Physical Science Basis. Contribution of Working Group I to the Fifth Assessment Report of the Intergovernmental Panel on Climate Change. . Cambridge University Press, Cambridge.

Jiang, Z., Lian, Y., Qin, X., 2014. Rocky desertification in Southwest China: impacts, causes, and restoration. Earth Sci. Rev. 132 (3), 1–12.

Konzelmann, T., et al., 1994. Parameterization of global and longwave incoming radiation for the Greenland Ice Sheet. Global Planet. Change 9 (1-2), 143–164.

Krishnamurti, T.N., et al., 2000. Multimodel ensemble forecasts for weather and seasonal climate. J. Clim. 13 (23), 4196–4216.

Lai, C., Chen, X., Wang, Z., et al., 2016. Spatio-temporal variation in rainfall erosivity during 1960–2012 in the Pearl River Basin, China. Catena 137, 382–391.

Li, Z., Zheng, F., Liu, W., 2012. Spatiotemporal characteristics of reference evapotranspiration during 1961–2009 and its projected changes during 2011–2099 on the Loess Plateau of China. Agric. For. Meteorol. 154 (-155), 147–155.

Liang, X., Lettenmaier, D.P., Wood, E.F., Burges, S.J., 1994. A simple hydrologically based model of land surface water and energy fluxes for general circulation models. J. Geophys. Res. Atmos. 99 (D7), 14415–14428.

Liang, X., Wood, E.F., Lettenmaier, D.P., 1996. Surface soil moisture parameterization of the VIC-2L model: evaluation and modification. Global Planet. Change 13 (1-4), 195–206.

Liu, J., et al., 2005. Spatial and temporal patterns of China's cropland during 1990–2000: An analysis based on Landsat TM data. Remote Sensing Environ. 98 (4), 442–456.

Liu, Y., et al., 2015. A new physically based self-Calibrating palmer drought severity index and its performance evaluation. Water Resour. Manage. 29 (13), 4833–4847.

Liu, X., Liang, X., Li, X., et al., 2017. A future land use simulation model (FLUS) for simulating multiple land use scenarios by coupling human and natural effects. Landscape Urban Plan 168, 94–116.

Lobell, D.B., Costa-Roberts, J., 2011. Climate trends and global crop production since 1980. Science 333 (6042), 616–620.

Lohmann, D., Nolte Holube, R., Raschke, E., 1996. A large-scale horizontal routing model to be coupled to land surface parametrization schemes. Tellus 48 (5), 708–721.

Martinezlozano, J.A., Tena, F., Onrubia, J.E., Jdela, R., 1985. The historical evolution of

the Angstrom formula and its modifications: review and bibliography. Agric. Forest Meteorol. 33 (2), 109–128.
Min, S.K., Hense, A., 2006. A Bayesian approach to climate model evaluation and multi-model averaging with an application to global mean surface temperatures from IPCC AR4 coupled climate models. Geophys. Res. Lett. 33 (8), 153–172.
Moss, R.H., et al., 2010. The next generation of scenarios for climate change research and assessment. Nature 463 (7282), 747–756.
Murphy, J.M., et al., 2004. Quantification of modelling uncertainties in a large ensemble of climate change simulations. Nature 430 (7001), 768–772.
Niu, J., Chen, J., 2016. A wavelet perspective on variabilities of hydrological processes in conjunction with geomorphic analysis over the Pearl River basin in South China. J. Hydrol. 542 (2016), 392–409.
Niu, J., Chen, J., Sun, L., 2015. Exploration of drought evolution using numerical simulations over the Xijiang (West River) basin in South China. J. Hydrol. 526, 68–77.
Palmer, W.C., 1965. Meteorological Drought. U.S. department of Commerce Weather Bureau Research Paper.
Peng, S., et al., 2017. Spatiotemporal change and trend analysis of potential evapotranspiration over the Loess Plateau of China during 2011–2100. Agric. Forest Meteorol. 232, 89–105.
Piao, S., et al., 2010. The impacts of climate change on water resources and agriculture in China. Nature 467 (7311), 43.
Raftery, A.E., Gneiting, T., Balabdaoui, F., Polakowski, M., 2005. Using bayesian model averaging to calibrate forecast ensembles. Mon. Weather Rev. 133 (5), 1155–1174.
Saxton, K.E., Rawls, W.J., 2006. Soil water characteristic estimates by texture and organic matter for hydrologic solutions. Soil Sci. Soc. Am. J. 70 (5), 1569–1578.
Sheffield, J., Wood, E.F., 2008. Projected changes in drought occurrence under future global warming from multi-model, multi-scenario, IPCC AR4 simulations. Clim. Dyn. 31 (1), 79–105.
Sheffield, J., Wood, E.F., Roderick, M.L., 2012. Little change in global drought over the past 60 years. Nature 491 (7424), 435.
Shen, Y., Xiong, A., 2015. Validation and comparison of a new gauge-based precipitation analysis over mainland China. Int. J. Climatol. 36 (1), 252–265.
Taylor, K.E., Stouffer, R.J., Meehl, G.A., 2011. An overview of CMIP5 and the experiment design. Bull. Am. Meteorol. Soc. 93 (4), 485–498.
Touma, D., Ashfaq, M., Nayak, M.A., Kao, S.C., Diffenbaugh, N.S., 2015. A multi-model and multi-index evaluation of drought characteristics in the 21st century. J. Hydrol. 526, 196–207.
Trenberth, K.E., et al., 2014. Global warming and changes in drought. Nat. Clim. Change 4 (1), 17–22.
Venkataraman, K., Tummuri, S., Medina, A., Perry, J., 2016. 21st century drought outlook for major climate divisions of Texas based on CMIP5 multimodel ensemble: implications for water resource management. J. Hydrol. 534, 300–316.
Vicente-Serrano, S.M., Beguería, S., López moreno, J.I., 2010. A multiscalar drought index sensitive to global warming: the standardized precipitation evapotranspiration index. J. Clim. 23 (7), 1696–1718.
Wang, L., Chen, W., 2014. A CMIP5 multimodel projection of future temperature, precipitation, and climatological drought in China. Int. J. Climatol. 34 (6), 2059–2078.
Wang, D., Hejazi, M., Cai, X., Valocchi, A.J., 2011. Climate change impact on meteorological, agricultural, and hydrological drought in central Illinois. Water Resour. Res. 47 (9), 1995–2021.
Wang, W., et al., 2017a. Bayesian multi-model projection of irrigation requirement and water use efficiency in three typical rice plantation region of China based on CMIP5. Agric. Forest Meteorol. 232, 89–105.
Wang, Z., et al., 2017b. Spatiotemporal variability of reference evapotranspiration and contributing climatic factors in China during 1961–2013. J. Hydrol. 97–108.
Wang, G., 2005. Agricultural drought in a future climate: results from 15 global climate models participating in the IPCC 4th assessment. Clim. Dyn. 25 (7–8), 739–753.
Wells, N., Goddard, S., Hayes, M.J., 2004. A self-Calibrating palmer drought severity index. J. Clim. 17 (12), 2335–2351.
Werner, A.T., Cannon, A.J., 2015. Hydrologic extremes − an intercomparison of multiple gridded statistical downscaling methods. Hydrol. Earth Syst. Sci. Discuss. 12 (6), 6179–6239.
Wiltshire, A., et al., 2013. The importance of population, climate change and CO 2 plant physiological forcing in determining future global water stress. Global Environ. Change 23 (5), 1083–1097.
Wu, Z.Y., Lu, G.H., Wen, L., Lin, C.A., 2011. Reconstructing and analyzing China's fifty-nine year (1951–2009) drought history using hydrological model simulation. Hydrol. Earth Syst. Sci. 15 (9), 2881–2894.
Wu, C., Huang, G., Yu, H., Chen, Z., Ma, J., 2014. Impact of climate change on reservoir flood control in the upstream area of the beijiang river basin, south China. J. Hydrometeorol. 15 (6), 2203–2218.
Xie, Z., Yuan, F., Zheng, J., et al., 2007. Regional parameter estimation of the VIC land surface model: methodology and application to river basins in China. J. Hydrometeorol. 8 (3), 447–468.
Xu, K., et al., 2015. Spatio-temporal variation of drought in China during 1961–2012: A climatic perspective. J. Hydrol. 526 (3), 253–264.
Yan, D., Werners, S.E., Ludwig, F., Huang, H.Q., 2015. Hydrological response to climate change: the Pearl River, China under different RCP scenarios. J. Hydrol. Reg. Stud. 4, 228–245.
Yevjevich, V., Ingenieur, J., 1967. An Objective Approach to Definitions and Investigations of Continental Hydrologic Droughts. Water Resource Publ, Fort Collins.
Zhang, B., He, C., 2016. A Modified Water Demand Estimation Method for Drought Identification over Arid and Semiarid Regions. Agricultural and Forest Meteorology.
Zhang, B., et al., 2012a. Drought variation trends in different subregions of the Chinese Loess Plateau over the past four decades. Agric. Water Manage. 115 (115), 167–177.
Zhang, Q., Singh, V.P., Peng, J., Chen, Y.D., Li, J., 2012b. Spatial-temporal changes of precipitation structure across the Pearl River basin, China. J. Hydrol. 440–441 (11), 113–122.
Zhang, W., Jin, F.F., Zhao, J.X., Qi, L., Ren, H.L., 2013. The possible influence of a nonconventional el Niño on the severe autumn drought of 2009 in southwest China. J. Clim. 26 (21), 8392–8405.